

MSCloudCAM: Cross-Attention with Multi-Scale Context for Multispectral Cloud Segmentation

Md Abdullah Al Mazid, Liangdong Deng, Naphtali Rishe

School of Computing and Information Sciences

Florida International University

Abstract—Clouds remain a critical challenge in optical satellite imagery, hindering reliable analysis for environmental monitoring, land cover mapping, and climate research. To overcome this, we propose MSCloudCAM, a Cross-Attention with Multi-Scale Context Network tailored for multispectral and multi-sensor cloud segmentation. Our framework exploits the spectral richness of Sentinel-2 (CloudSEN12) and Landsat-8 (L8Biome) data to classify four semantic categories: clear sky, thin cloud, thick cloud, and cloud shadow. MSCloudCAM combines a Swin Transformer backbone for hierarchical feature extraction with multi-scale context modules—ASPP and PSP—for enhanced scale-aware learning. A Cross-Attention block enables effective multisensor and multispectral feature fusion, while the integration of an Efficient Channel Attention Block (ECAB) and a Spatial Attention Module adaptively refine feature representations. Comprehensive experiments on CloudSEN12 and L8Biome demonstrate that MSCloudCAM delivers state-of-the-art segmentation accuracy, surpassing leading baseline architectures while maintaining competitive parameter efficiency and FLOPs. These results underscore the model’s effectiveness and practicality, making it well-suited for large-scale Earth observation tasks and real-world applications.

Index Terms—Cloud segmentation, multispectral imagery, deep learning, cross attention, multi-scale context, Sentinel-2, Landsat-8

I. INTRODUCTION

Clouds significantly obscure the Earth’s surface in optical satellite imagery, creating persistent challenges for remote sensing applications. Accurate detection and classification of cloud types are essential for atmospheric correction, land surface monitoring, and environmental modeling.

Current deep learning-based cloud masking and segmentation methods have demonstrated strong performance by leveraging hierarchical feature representations. However, most existing approaches remain limited in their ability to generalize across different sensors and spectral configurations. This limitation becomes especially critical in **multi-class scenarios** that require discriminating between *thin clouds*, *thick clouds*, and *cloud shadows*, where subtle spectral and spatial variations are often misclassified.

We propose **MSCloudCAM**, a novel architecture designed for robust cloud segmentation in multispectral, multi-sensor imagery. The model exploits multi-scale context encoding and cross attention to effectively fuse complementary features from different resolutions and spectral domains, enabling accurate pixel-wise classification across heterogeneous datasets.

Our key contributions are as follows:

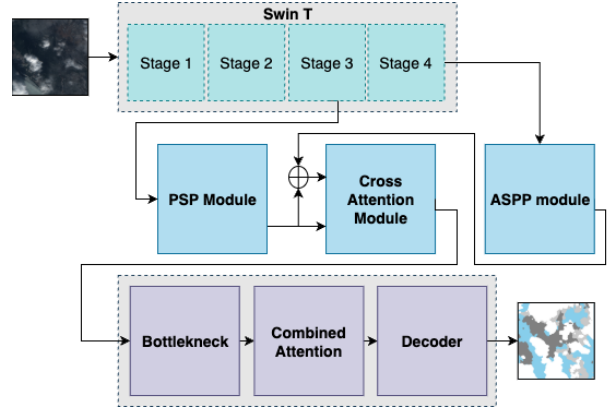


Fig. 1. High-level architecture of **MSCloudCAM**. The model integrates a Swin Transformer backbone with ASPP and PSP for multi-scale context, and incorporates a Cross Attention module for robust feature fusion across Sentinel-2 and Landsat-8 imagery.

- We develop a hybrid backbone that integrates the Swin Transformer [1] with ASPP [2] and PSP [3] modules, enabling comprehensive multi-scale context aggregation.
- We introduce a **Cross Attention module** that enhances feature fusion between high-level semantic and mid-level spatial features, improving robustness in complex cloud scenarios.
- We demonstrate that MSCloudCAM achieves superior performance on both Sentinel-2 (CloudSEN12) [4] and Landsat-8 (L8Biome) [5] imagery, consistently outperforming strong state-of-the-art segmentation networks while maintaining computational efficiency.

II. RELATED WORK

A. Cloud Segmentation in Remote Sensing

Cloud segmentation in optical satellite imagery has long been studied due to its importance in atmospheric correction, land cover mapping, and environmental monitoring. Early **rule-based methods**, such as Fmask [6], applied band-specific thresholds and decision trees (e.g., cirrus, TIR bands in Landsat) but often misclassified *mixed pixels*, *thin clouds*, and bright surfaces like snow or sand [7].

Spectral index-based approaches leveraged indices such as NDSI, NDVI, and cloud probability measures [8], offering more robustness than simple thresholds but still failing under high spectral variability or semi-transparent clouds.

Later, **machine learning classifiers** (SVMs, Random Forests, gradient boosting) [9] combined spectral and textural features, improving accuracy but remaining limited by handcrafted inputs and shallow context modeling. These shortcomings motivated the transition to deep learning, which directly learns multi-scale, discriminative features from raw multispectral data.

B. Deep Learning Approaches

Deep learning has become the dominant paradigm for cloud segmentation in remote sensing, offering substantial improvements in accuracy, robustness, and generalization compared to traditional threshold-based methods.

CNN-based architectures remain foundational in this domain due to their strong spatial feature extraction capabilities and hierarchical representation learning. Encoder-decoder designs such as *UNet* [10] and its lightweight adaptation *UNetMoby2* [11] preserve fine-grained localization via skip connections, making them effective for delineating cloud boundaries. *DeepLabV3+* [2] enhances context capture through atrous convolutions and the Atrous Spatial Pyramid Pooling (ASPP) module, enabling multi-scale feature aggregation for detecting clouds of varying thickness. Several CNN variants have been developed specifically for cloud detection, including *CDNetv1* [12] and *CDNetv2* [13] with spectral index integration and multi-branch architectures, *KappaMask* [14] incorporating Kappa coefficient-based loss for class imbalance handling, *DBNet* [15] using dual-branch feature extraction for spatial-spectral fusion, *SCNN* [16] employing spectral-spatial separable convolutions, *MCDNet* [17] with multi-channel dense connections, and *HRCloudNet* [18] designed for high-resolution imagery.

Transformer-based architectures leverage self-attention mechanisms to capture long-range dependencies, a property highly beneficial for clouds that span large spatial extents or exhibit non-local spectral correlations. *SegFormer* [19] combines the lightweight MixVision Transformer (MiT) backbone with an MLP decoder for efficient global context modeling. *Mask2Former* [20] unifies instance, semantic, and panoptic segmentation through masked attention, offering strong adaptability to heterogeneous cloud patterns. *UPerNet-InternImage* [21] integrates a hierarchical transformer backbone (InternImage) with pyramid pooling for multi-scale representation, achieving state-of-the-art results on multiple remote sensing segmentation benchmarks.

Hybrid architectures aim to combine the strengths of CNNs and transformers by using CNN layers for low-level texture and spectral edge extraction, followed by transformer modules for global reasoning. Examples include HRNet-Transformer hybrids and cross-attention fusion models [1], which have been applied to atmospheric feature segmentation.

Foundation model-based segmentation has recently emerged as a promising direction, adapting large-scale pre-trained vision transformers such as *DINOv2* [22] for remote sensing segmentation. These models are trained on massive, diverse datasets and provide rich, generalizable features. While

they have demonstrated strong zero-shot and fine-tuned performance in RGB domains, their adaptation to multispectral or multi-sensor data requires spectral-specific preprocessing and fine-tuning strategies.

Despite these advances, most existing models are trained and evaluated on *single-sensor datasets*, limiting their ability to generalize across multi-sensor imagery. Moreover, few explicitly integrate *multi-scale spectral-spatial features with cross-attention mechanisms* tailored for cloud segmentation. Our proposed MSCloudCAM addresses both gaps by combining a Swin Transformer [1] backbone with ASPP [2] and PSP [3] modules for multi-scale context aggregation, a Cross Attention block for sensor fusion, and ECAB [23] and spatial attention [24], [25] for adaptive feature refinement.

C. Gaps in Current Methods

Despite progress, most existing networks are trained on single-sensor datasets, limiting generalization to multi-sensor scenarios. Additionally, few works explicitly integrate multi-scale spectral-spatial features with cross-attention mechanisms for cloud segmentation. Our MSCloudCAM addresses both these gaps.

III. METHODOLOGY

A. Overview

MSCloudCAM is a multispectral semantic segmentation network that integrates a Swin Transformer encoder with dual context modules, a cross-attention fusion mechanism, and a lightweight combined attention refinement block. The model is designed to capture long-range spectral-spatial dependencies while retaining fine-grained local structure. A multi-stage decoder with auxiliary supervision produces the final dense predictions. The overall pipeline is illustrated in Fig. 2.

B. Backbone Feature Extraction

Let $\mathbf{X} \in \mathbb{R}^{B \times C_{\text{in}} \times H_0 \times W_0}$ denote the input multispectral image with C_{in} spectral channels (13 for Sentinel-2, 11 for Landsat-8). The Swin Transformer encoder $\mathcal{E}(\cdot)$ produces a hierarchy of features:

$$\{f_1, f_2, f_3, f_4\} = \mathcal{E}(\mathbf{X}), \quad f_i \in \mathbb{R}^{B \times C_i \times H_i \times W_i}, \quad (1)$$

with channel dimensions [96, 192, 384, 768] and progressively reduced spatial sizes (H_i, W_i) . Shifted-window self-attention within Swin ensures that f_4 captures global dependencies, while f_1-f_3 preserve finer detail.

C. Multi-Scale Context Modules

To enhance representational richness, we employ two complementary context encoders that operate at different feature hierarchies.

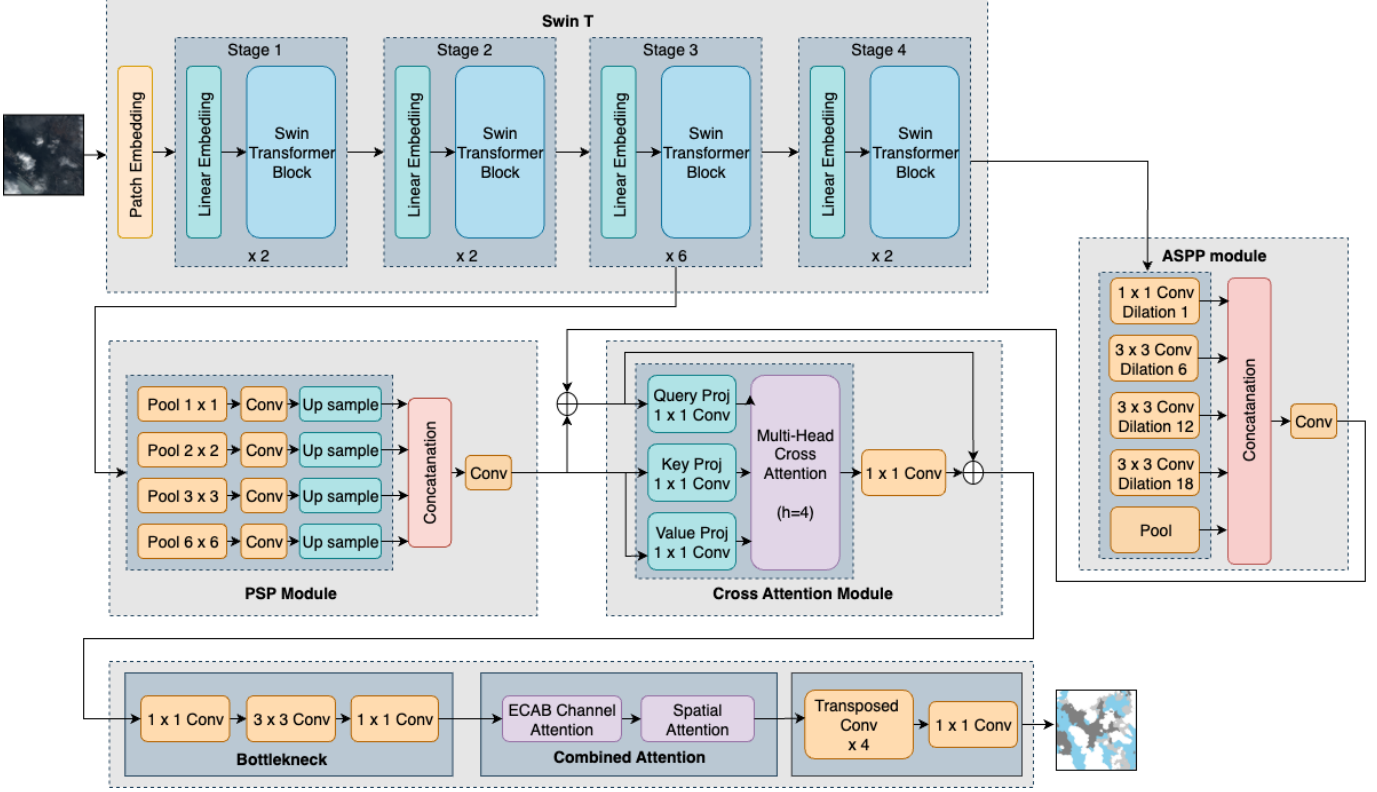


Fig. 2. Architecture of MSCloudCAM. A multispectral Swin Transformer encoder generates hierarchical features. ASPP and PSP modules enrich deep and intermediate representations. These are fused by convolutional cross-attention, refined via channel–spatial attention, and decoded by a multi-stage upsampling path with auxiliary supervision.

ASPP [2]: Applied to the deepest feature map f_4 , Atrous Spatial Pyramid Pooling expands the effective receptive field through parallel dilated convolutions with multiple rates and an additional global context branch:

$$x_{\text{ASPP}} = \phi_{\text{ASPP}}(f_4) = \bigoplus_{r \in \{1, 6, 12, 18\}} \sigma(\text{Conv}_{3 \times 3}^{(r)}(f_4)) \oplus \sigma(\text{GAP}(f_4)), \quad (2)$$

where \oplus denotes channel-wise concatenation, r specifies the dilation rate, GAP is global average pooling, and σ represents the ReLU nonlinearity. This module injects large-scale semantic context while retaining spatial discrimination.

PSP [3]: For the intermediate feature map f_3 , Pyramid Scene Parsing aggregates multi-scale contextual cues by adaptive pooling at several grid scales:

$$x_{\text{PSP}} = \phi_{\text{PSP}}(f_3) = \bigoplus_{s \in \{1, 2, 3, 6\}} \sigma(\text{Up}(\text{Pool}_s(f_3))), \quad (3)$$

where Pool_s denotes average pooling to an $s \times s$ grid, followed by projection and bilinear upsampling. This captures scene-level information at progressively coarser scales, which is essential for delineating fine structures such as thin clouds.

D. Cross-Attention Fusion

The ASPP and PSP outputs are concatenated to form a joint query representation:

$$x_{\text{cat}} = [x_{\text{ASPP}} \parallel x_{\text{PSP}}] \in \mathbb{R}^{B \times (C_a + C_p) \times H \times W}. \quad (4)$$

A convolutional multi-head cross-attention module then refines this fused tensor by treating x_{PSP} as contextual guidance:

$$Q = W_Q * x_{\text{cat}}, \quad (5)$$

$$K = W_K * x_{\text{PSP}}, \quad (6)$$

$$V = W_V * x_{\text{PSP}}, \quad (7)$$

$$\text{Attn}(Q, K, V) = \text{softmax}\left(\frac{QK^\top}{\sqrt{d_k}}\right)V, \quad (8)$$

$$\tilde{x} = W_O * \text{Attn}(Q, K, V) + x_{\text{cat}}. \quad (9)$$

Here, $*$ denotes convolution, d_k is the per-head dimension, and residual addition ensures stable learning. This mechanism aligns global semantics from ASPP with fine-grained spatial cues from PSP.

TABLE I
PERFORMANCE COMPARISON ON CLOUDSEN12 L1C (TOA).

Model	IoU (%)						F1 (%)				Accuracy (%)					aAcc (%)
	Clear	Thick	Thin	Shadow	mIoU	Clear	Thick	Thin	Shadow	mF1	Clear	Thick	Thin	Shadow	mAcc	
DBNet [15]	85.20	43.02	81.40	52.44	65.52	92.01	60.16	89.75	68.80	77.68	95.56	53.15	89.40	62.47	75.15	86.83
CDNetv2 [13]	84.98	43.37	80.67	53.40	65.60	91.88	60.50	89.30	69.62	77.83	94.80	53.13	89.32	65.34	75.65	86.68
HRCloudNet [18]	86.01	45.88	83.54	57.61	68.26	92.48	62.90	91.03	73.10	79.88	94.49	59.47	91.39	67.19	78.13	87.86
U-Net-MobV2	90.82	85.98	50.54	67.21	73.64	95.19	92.46	67.14	80.39	83.80	94.42	96.11	95.05	96.62	95.55	91.10
U-Net++-MobV2	90.93	86.58	49.78	66.93	73.56	95.25	92.81	66.47	80.19	83.68	94.47	96.25	95.27	96.56	95.64	91.28
DeepLabV3+-MobV2	90.13	85.75	48.97	66.29	72.79	94.81	92.33	65.75	79.73	83.15	94.02	96.04	94.53	96.51	95.28	90.55
U-Net-ResNet101	90.62	86.16	47.15	66.05	72.50	95.08	92.56	64.08	79.56	82.82	94.24	96.13	94.97	96.57	95.48	90.95
U-Net++-ResNet101	90.90	86.43	46.24	68.46	73.01	95.23	92.72	63.24	81.27	83.12	94.45	96.16	95.06	96.74	95.60	91.20
DeepLabV3+-ResNet101	90.65	85.66	50.60	66.36	73.32	95.10	92.28	67.20	79.78	83.59	94.38	95.94	94.94	96.47	95.43	90.87
UPerNet-InternImage	90.85	85.28	36.70	68.87	70.42	95.09	91.82	47.94	80.98	78.96	94.50	96.43	95.24	96.85	95.75	91.51
Mask2Former-DINOv2	88.50	82.10	43.61	63.62	69.46	93.90	90.17	60.73	77.76	80.64	92.94	94.84	94.41	96.11	94.57	89.15
Mask2Former-Swin-T	90.75	86.70	49.90	69.53	74.22	95.15	92.88	66.58	82.02	84.16	94.46	96.32	94.34	96.93	95.51	91.03
SegFormer-MiT-B5	91.47	86.70	49.77	70.24	74.54	95.55	92.88	66.46	82.52	84.35	94.84	96.27	95.25	96.92	95.82	91.64
MSCloudCAM	91.64	87.24	52.58	70.63	75.52	95.64	93.19	68.92	82.78	85.13	94.93	96.42	95.58	97.04	95.99	91.99

E. Bottleneck Projection

The fused representation \tilde{x} is compressed and regularized through a three-layer bottleneck:

$$\begin{aligned} z &= \phi_{\text{bottleneck}}(\tilde{x}) \\ &= \sigma\left(\text{Conv}_{1 \times 1}(\sigma(\text{Conv}_{3 \times 3}(\sigma(\text{Conv}_{1 \times 1}(\tilde{x})))))\right), \end{aligned} \quad (10)$$

which first reduces dimensionality, then captures local spatial dependencies, and finally projects features into a compact 512-channel embedding. This step reduces redundancy and prepares the representation for attention-based refinement.

F. Combined Attention Refinement

The bottleneck output z is recalibrated by a combined attention operator:

$$z' = \phi_{\text{CA}}(z) = \phi_{\text{ECA}}(z) \odot \phi_{\text{SA}}(z) + z, \quad (11)$$

where ϕ_{ECA} denotes Efficient Channel Attention [23] and ϕ_{SA} is spatial attention [24], [25], and \odot is element-wise multiplication. This highlights discriminative regions while preserving residual information.

G. Decoder with Deep Supervision

The refined representation z' is progressively upsampled through transposed convolutions:

$$y_i = \sigma(\text{Deconv}_i(y_{i-1})), \quad i = 1, \dots, 4, \quad (12)$$

with $y_0 = z'$. Two intermediate outputs, \hat{Y}_1 and \hat{Y}_2 , are generated from y_1 and y_2 , respectively, and resized to the input resolution (H_0, W_0) . The final prediction \hat{Y} is obtained from y_4 . The training objective jointly supervises all three outputs:

$$\mathcal{L} = \lambda_{\text{final}}\mathcal{L}(\hat{Y}, Y) + \lambda_1\mathcal{L}(\hat{Y}_1, Y) + \lambda_2\mathcal{L}(\hat{Y}_2, Y), \quad (13)$$

where Y is the ground truth mask, and $(\lambda_{\text{final}}, \lambda_1, \lambda_2)$ are supervision weights.

IV. EXPERIMENTS

A. Datasets

We evaluate MSCloud on two publicly available multispectral cloud segmentation datasets.

CloudSEN12 [4] is a global Sentinel-2 cloud segmentation dataset with 13 spectral bands (10–60 m) and pixel-level labels for *clear* (0), *thick cloud* (1), *thin cloud* (2), and *cloud shadow* (3). We use the *high* subset, selecting 10k samples each from L1C and L2A. All bands are normalized by dividing top-of-atmosphere reflectance by 3000.0.

L8Biome [5] is derived from Landsat-8 CCA, containing 11 bands (30 m) with manual masks. The original five classes—*fill* (0), *shadow* (64), *clear* (128), *thin cloud* (192), and *cloud* (255)—are remapped to CloudSEN12’s taxonomy: *clear* \rightarrow 0, *thick cloud* \rightarrow 1, *thin cloud* \rightarrow 2, *shadow* \rightarrow 3. The *fill* class is ignored. Bands are normalized with the same 3000.0 divisor for consistency.

TABLE II
DATASET SPLIT STATISTICS FOR CLOUDSEN12 AND L8BIOME.

Dataset	Train	Validation	Test
CloudSEN12 L1C	8,500	500	1,000
CloudSEN12 L2A	8,500	500	1,000
L8Biome	13,378	4,459	4,459

B. Loss Function

The training objective is a weighted sum of the losses from the final prediction and the two auxiliary predictions:

$$\mathcal{L} = \lambda_{\text{final}}\mathcal{L}_{\text{final}} + \lambda_1\mathcal{L}_1 + \lambda_2\mathcal{L}_2. \quad (14)$$

We set $\lambda_{\text{final}} = 1.0$ and $\lambda_1 = \lambda_2 = 0.4$, ensuring the final prediction dominates while auxiliary supervision stabilizes early-stage training.

C. Training Protocol

Our model is trained using the Adam optimizer with an initial learning rate of 1×10^{-4} . The batch size is set to 8, and we train for 100 epochs.

TABLE III
PERFORMANCE COMPARISON ON CLOUDSEN12 L2A (BOA).

Model	IoU (%)					F1 (%)					Accuracy (%)					aAcc (%)
	Clear	Thick	Thin	Shadow	mIoU	Clear	Thick	Thin	Shadow	mF1	Clear	Thick	Thin	Shadow	mAcc	
DBNet [15]	85.42	42.76	80.80	53.62	65.65	92.14	59.90	89.38	69.81	77.81	94.83	53.53	90.27	63.45	75.52	86.82
CDNetv2 [13]	85.35	44.01	80.85	54.00	66.05	92.09	61.12	89.41	70.13	78.19	95.65	56.37	88.06	63.56	75.91	86.88
HRCloudNet [18]	87.24	44.18	82.78	59.20	68.35	93.19	61.28	90.58	74.37	79.85	95.41	51.00	93.17	69.83	77.35	88.35
U-Net-MobV2	88.74	83.87	54.13	60.15	71.72	94.03	91.23	70.24	75.12	82.65	93.45	95.55	93.71	95.43	94.53	89.07
U-Net++-MobV2	87.45	83.33	50.70	57.62	69.78	93.30	90.91	67.29	73.11	81.15	92.52	95.47	93.26	95.23	94.12	88.23
DeepLabV3+-MobV2	88.01	83.70	50.36	61.78	70.96	93.62	91.12	66.98	76.37	82.03	92.93	95.46	93.83	95.45	94.42	88.84
U-Net-ResNet101	86.51	81.76	37.12	58.89	66.07	92.77	89.97	54.14	74.12	77.75	91.83	94.73	92.76	95.13	93.61	87.23
U-Net++-ResNet101	87.85	81.03	47.47	59.12	68.87	93.53	89.52	64.38	74.31	80.44	92.84	94.47	93.39	95.37	94.02	88.04
DeepLabV3+-ResNet101	87.96	82.83	50.36	59.52	70.17	93.59	90.61	66.99	74.63	81.45	92.93	95.15	93.79	95.14	94.25	88.50
UPerNet-InternImage	87.79	82.22	40.31	63.96	68.57	93.30	89.78	51.63	77.19	77.98	93.08	95.55	93.48	95.50	94.40	88.81
Mask2Former-DINOv2	83.53	79.32	45.51	56.50	66.21	91.03	88.47	62.55	72.21	78.56	90.30	94.23	91.17	94.93	92.66	85.31
Mask2Former-Swin-T	88.91	84.35	50.72	63.25	71.81	94.13	91.51	67.30	77.49	82.61	93.61	95.77	93.33	95.30	94.50	89.01
SegFormer-MiT-B5	89.28	83.50	51.87	64.19	72.21	94.34	91.01	68.31	78.19	82.96	93.76	95.36	93.86	95.90	94.72	89.44
MSCloudCAM	89.28	84.30	55.53	63.38	73.12	94.33	91.48	71.40	77.58	83.70	93.76	95.69	94.20	95.74	94.85	89.69

D. Evaluation Metrics

a) Per-class Metrics.:

$$\text{IoU}_i = \frac{\text{TP}_i}{\text{TP}_i + \text{FP}_i + \text{FN}_i}, \quad (15)$$

$$\text{F1}_i = \frac{2\text{TP}_i}{2\text{TP}_i + \text{FP}_i + \text{FN}_i}, \quad (16)$$

$$\text{Acc}_i = \frac{\text{TP}_i + \text{TN}_i}{\text{TP}_i + \text{FP}_i + \text{FN}_i + \text{TN}_i}. \quad (17)$$

Per-class metrics (IoU_i , F1_i , Acc_i) evaluate individual categories, while their means (mIoU, mF1, mAcc) are obtained by averaging across K classes, giving equal weight regardless of class size. In contrast, overall accuracy (aAcc) is computed over all pixels, thus weighting larger classes more heavily.

b) *Ignored labels.*: Pixels with sentinel values (e.g., *Fill* in L8Biome) are removed from \mathbf{C} and all denominators via an `ignore_index` mask, ensuring metrics are based on identical valid-pixel sets.

c) *Reporting.*: We report class-wise IoU and F1 (*clear*, *thick cloud*, *thin cloud*, *cloud shadow*), together with mIoU, mDice, mAcc, and aAcc. Unless noted, averages are macro over classes.

V. RESULTS

A. Quantitative Performance

We first evaluate the models quantitatively in terms of IoU, F1, and Accuracy on three benchmark datasets (CloudSEN12 L1C, CloudSEN12 L2A, and L8Biome). Tables I–IV present the detailed results.

B. Qualitative Results

To further illustrate the effectiveness of the proposed method, we present visual comparisons of cloud segmentation results in Fig. 3. Each **row** corresponds to a different dataset, and each **column** corresponds to a different segmentation method. As shown in the figure, the proposed method produces more accurate delineation of thin clouds and cloud shadows, while reducing false detections compared to the baseline approaches.

C. Model Complexity Analysis

Table V summarizes the computational complexity of all evaluated models in terms of FLOPs and parameter counts. While some architectures (e.g., UPerNet-InternImage and Mask2Former-DINOv2) exhibit significantly higher complexity, our proposed **MSCloudCAM** achieves a favorable trade-off between accuracy and efficiency. Specifically, MSCloudCAM attains competitive performance while requiring fewer FLOPs than SegFormer-MiT-B5, and substantially fewer FLOPs than UPerNet-InternImage, with a moderate parameter count.

TABLE V
MODEL COMPLEXITY COMPARISON IN TERMS OF FLOPS AND PARAMETERS.

Model	FLOPs (G)	Parameters (M)
U-Net-MobileNetV2	13.613	6.629
U-Net++-MobileNetV2	18.023	6.825
DeepLabV3+-MobileNetV2	6.057	4.379
U-Net-ResNet101	62.258	51.514
U-Net++-ResNet101	250.000	67.978
DeepLabV3+-ResNet101	56.192	45.670
UPerNet-InternImage-B-DCNv4	200–250	100–130
Mask2Former-Swin-T	73.090	47.400
Mask2Former-DINOv2-ViT-B/14	75–95	87–92
SegFormer-MiT-B5	55.430	45.652
MSCloudCAM	38.98	47.44

VI. CODE AND MODEL AVAILABILITY

The full implementation of our proposed **MS-CloudCAM** framework is publicly available. The source code, training scripts, and experimental configurations are hosted on GitHub: <https://github.com/mazid-rafee/ms-cloudcam>. Additionally, pre-trained model checkpoints are released on Hugging Face: <https://huggingface.co/mazid-rafee/MS-CloudCAM/tree/main>.

VII. CONCLUSION

We presented MSCloudCAM, a cross attention with multi-scale context network for multispectral, multi-sensor cloud segmentation. By integrating transformer-based backbones with multi-scale context and attention mechanisms, our method achieves superior segmentation accuracy over strong baselines on CloudSEN12 and L8Biome datasets. Future work will

TABLE IV
PERFORMANCE COMPARISON ON **L8BIOME**.

Model	IoU (%)					F1 (%)				Accuracy (%)				aAcc (%)		
	Clear	Thick	Thin	Shadow	mIoU	Clear	Thick	Thin	mF1	Clear	Thick	Thin	Shadow	mAcc		
CDNetv2 [13]	73.81	24.85	75.85	0.00	43.63	84.93	39.81	86.27	0.00	52.75	90.18	31.95	89.81	0.00	52.98	78.56
HRCloudNet [18]	72.41	30.89	70.76	0.00	43.51	83.99	47.20	82.88	0.00	53.52	85.50	43.70	85.88	0.00	53.77	77.04
DBNet [15]	80.19	38.18	82.37	0.49	51.41	89.00	55.25	90.34	0.93	60.99	96.51	49.34	87.89	0.50	59.70	83.62
U-Net-MobV2	88.98	78.59	39.97	6.37	53.48	94.17	88.01	57.11	11.98	62.82	94.26	91.50	87.55	98.55	92.97	85.93
U-Net++-MobV2	88.96	81.68	39.44	4.42	53.62	94.16	89.91	56.57	8.47	62.28	94.13	93.55	88.76	98.57	93.55	87.09
DeepLabV3+-MobV2	87.25	79.21	33.37	2.54	50.59	93.19	88.40	50.05	4.96	59.15	93.32	91.25	87.50	98.54	92.65	85.31
U-Net-ResNet101	84.29	77.00	30.56	1.25	48.28	91.47	87.01	46.81	2.48	56.94	91.30	90.94	86.06	98.01	91.58	83.16
U-Net++-ResNet101	88.16	80.23	34.94	3.81	51.78	93.71	89.03	51.78	7.34	60.46	93.73	91.94	87.87	98.52	93.01	86.03
DeepLabV3+-ResNet101	87.56	74.19	34.24	4.88	50.22	93.37	85.18	51.01	9.31	59.72	93.47	89.56	85.51	98.56	91.78	83.55
UPerNet-InternImage	54.68	46.97	18.65	1.56	30.46	60.19	53.40	26.72	2.55	35.72	91.00	90.58	83.73	98.35	90.92	81.83
Mask2Former-DINOv2	69.67	70.75	34.67	13.13	47.06	82.12	82.87	51.49	23.22	59.93	84.03	86.86	84.39	98.65	88.48	76.96
Mask2Former-Swin-T	84.36	78.64	37.50	13.54	53.51	91.52	88.04	54.55	23.85	64.49	91.74	91.62	86.01	98.62	92.00	84.00
SegFormer-MiT-B5	88.62	74.38	39.52	15.27	54.45	93.97	85.31	56.65	26.50	65.61	94.04	90.12	86.05	98.70	92.23	84.45
MsCloudCAM	88.27	82.23	40.19	21.48	58.04	93.77	90.25	57.34	35.36	69.18	93.84	92.91	88.74	98.70	93.55	87.09

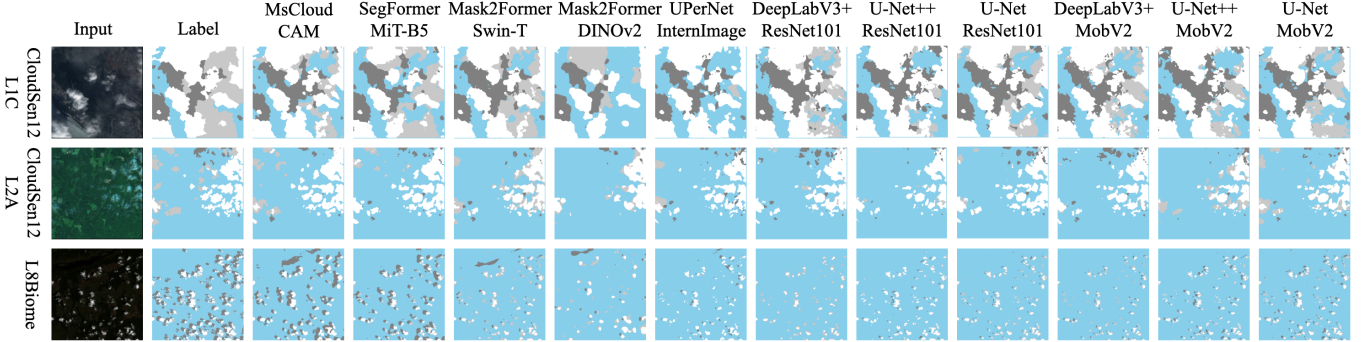


Fig. 3. Qualitative cloud segmentation results. Each row corresponds to a dataset. The proposed method produces sharper delineation of thin clouds and shadows compared to other approaches. Class-color mapping: Class 1 (Clear sky – light blue), Class 2 (Thick cloud – white), Class 3 (Thin cloud – light gray), Class 4 (Cloud shadow – dark gray).

explore lightweight variants for onboard satellite processing and extend the model to spatiotemporal cloud tracking.

ACKNOWLEDGMENT

This material is based in part upon work supported by the National Science Foundation under Grants CNS-2018611 and CNS-1920182.

REFERENCES

- [1] Z. Liu, Y. Lin, Y. Cao, H. Hu, Y. Wei, Z. Zhang, S. Lin, and B. Guo, “Swin transformer: Hierarchical vision transformer using shifted windows,” in *Proceedings of the IEEE/CVF International Conference on Computer Vision*, 2021, pp. 10 012–10 022.
- [2] L.-C. Chen, Y. Zhu, G. Papandreou, F. Schroff, and H. Adam, “Encoder-decoder with atrous separable convolution for semantic image segmentation,” in *Proceedings of the European Conference on Computer Vision (ECCV)*, 2018, pp. 801–818.
- [3] H. Zhao, J. Shi, X. Qi, X. Wang, and J. Jia, “Pyramid scene parsing network,” in *Proceedings of the IEEE Conference on Computer Vision and Pattern Recognition*, 2017, pp. 2881–2890.
- [4] C. Aybar, L. Ysuhuaylas, J. Loja, K. Gonzales, F. Herrera, L. Bautista, R. Yali, A. Flores, L. Diaz, N. Cuenca *et al.*, “CloudSEN12, a global dataset for semantic understanding of cloud and cloud shadow in Sentinel-2,” *Scientific Data*, vol. 9, no. 1, p. 782, 2022.
- [5] S. Foga, P. L. Scaramuzza, S. Guo, Z. Zhu, R. D. Dilley Jr, T. Beckmann, G. L. Schmidt, J. L. Dwyer, M. J. Hughes, and B. Laue, “Cloud detection algorithm comparison and validation for operational Landsat data products,” *Remote Sensing of Environment*, vol. 194, pp. 379–390, 2017.
- [6] Z. Zhu and C. E. Woodcock, “Object-based cloud and cloud shadow detection in Landsat imagery,” *Remote Sensing of Environment*, vol. 118, pp. 83–94, 2012.
- [7] Z. Zhu and C. E. Woodcock, “Automated cloud, cloud shadow, and snow detection in multitemporal Landsat data: An algorithm designed specifically for monitoring land cover change,” *Remote Sensing of Environment*, vol. 152, pp. 217–234, 2014.
- [8] A. Hollstein, K. Segl, L. Guanter, M. Brell, and M. Enesco, “Ready-to-use methods for the detection of clouds, cirrus, snow, shadow, water and clear sky pixels in Sentinel-2 MSI images,” *Remote Sensing*, vol. 8, no. 8, p. 666, 2016.
- [9] R. Singh, M. Biswas, and M. Pal, “Cloud detection using Sentinel 2 imageries: a comparison of XGBoost, RF, SVM, and CNN algorithms,” *Geocarto International*, pp. 1–32, 2022.
- [10] O. Ronneberger, P. Fischer, and T. Brox, “U-net: Convolutional networks for biomedical image segmentation,” in *International Conference on Medical Image Computing and Computer-assisted Intervention*. Springer, 2015, pp. 234–241.
- [11] M. Sandler, A. Howard, M. Zhu, A. Zhmoginov, and L.-C. Chen, “Mobilenetv2: Inverted residuals and linear bottlenecks,” in *Proceedings of the IEEE Conference on Computer Vision and Pattern Recognition*, 2018, pp. 4510–4520.
- [12] J. Yang, J. Guo, H. Yue, Z. Liu, H. Hu, and K. Li, “CDnet: CNN-based cloud detection for remote sensing imagery,” *IEEE Transactions on Geoscience and Remote Sensing*, vol. 57, no. 8, pp. 6195–6211, 2019.

- [13] J. Guo, J. Yang, H. Yue, H. Tan, C. Hou, and K. Li, “CDnetV2: CNN-based cloud detection for remote sensing imagery with cloud-snow coexistence,” *IEEE Transactions on Geoscience and Remote Sensing*, vol. 59, no. 1, pp. 700–713, 2020.
- [14] M. Domnich, I. Sünter, H. Trofimov, O. Wold, F. Harun, A. Kostiukhin, M. Järveoja, M. Veske, T. Tamm, K. Voormansik *et al.*, “KappaMask: AI-based cloudmask processor for Sentinel-2,” *Remote Sensing*, vol. 13, no. 20, p. 4100, 2021.
- [15] C. Lu, M. Xia, M. Qian, and B. Chen, “Dual-branch network for cloud and cloud shadow segmentation,” *IEEE Transactions on Geoscience and Remote Sensing*, vol. 60, pp. 1–12, 2022.
- [16] D. Chai, J. Huang, M. Wu, X. Yang, and R. Wang, “Remote sensing image cloud detection using a shallow convolutional neural network,” *ISPRS Journal of Photogrammetry and Remote Sensing*, vol. 209, pp. 66–84, 2024.
- [17] J. Dong, Y. Wang, Y. Yang, M. Yang, and J. Chen, “MCDNet: Multilevel cloud detection network for remote sensing images based on dual-perspective change-guided and multi-scale feature fusion,” *International Journal of Applied Earth Observation and Geoinformation*, vol. 129, p. 103820, 2024.
- [18] J. Li, T. Xue, J. Zhao, J. Ge, Y. Min, W. Su, and K. Zhan, “High-resolution cloud detection network,” *Journal of Electronic Imaging*, vol. 33, no. 4, pp. 043 027–043 027, 2024.
- [19] E. Xie, W. Wang, Z. Yu, A. Anandkumar, J. M. Alvarez, and P. Luo, “SegFormer: Simple and efficient design for semantic segmentation with transformers,” *Advances in Neural Information Processing Systems*, vol. 34, pp. 12 077–12 090, 2021.
- [20] B. Cheng, I. Misra, A. G. Schwing, A. Kirillov, and R. Girdhar, “Masked-attention mask transformer for universal image segmentation,” in *Proceedings of the IEEE/CVF Conference on Computer Vision and Pattern Recognition*, 2022, pp. 1290–1299.
- [21] W. Wang, J. Dai, Z. Chen, Z. Huang, Z. Li, X. Zhu, X. Hu, T. Lu, L. Lu, H. Li *et al.*, “Internimage: Exploring large-scale vision foundation models with deformable convolutions,” in *Proceedings of the IEEE/CVF Conference on Computer Vision and Pattern Recognition*, 2023, pp. 14 408–14 419.
- [22] M. Oquab, T. Darct, T. Moutakanni *et al.*, “DINOv2: Learning Robust Visual Features without Supervision,” *Transactions on Machine Learning Research*, pp. 1–31, 2024.
- [23] Q. Wang, B. Wu, P. Zhu, P. Li, W. Zuo, and Q. Hu, “ECA-Net: Efficient channel attention for deep convolutional neural networks,” in *Proceedings of the IEEE/CVF Conference on Computer Vision and Pattern Recognition*, 2020, pp. 11 534–11 542.
- [24] S. Woo, J. Park, J.-Y. Lee, and I. S. Kweon, “Cbam: Convolutional block attention module,” in *Proceedings of the European Conference on Computer Vision (ECCV)*, 2018, pp. 3–19.
- [25] T. Liu, R. Luo, L. Xu, D. Feng, L. Cao, S. Liu, and J. Guo, “Spatial channel attention for deep convolutional neural networks,” *Mathematics*, vol. 10, no. 10, p. 1750, 2022.